2014

Computational challenges for simulations related to the NASA electric arc shock tube (EAST) experiments

Dmitry V. Kotov
Stanford Center for Turbulence Research, dkotov@stanford.edu

Helen C. Yee
NASA Ames Research Center, yee@nas.nasa.gov

Marco Panesi
University of Illinois at Urbana-Champaign, mpanesi@illinois.edu

Dinesh K. Prabhu
NASA Ames Research Center, dinesh.k.prabhu@nasa.gov

Alan A. Wray
NASA Ames Research Center, alan.a.wray@nasa.gov

Journal of Computational Physics 269 (2014) 215–233

Contents lists available at ScienceDirect

Journal of Computational Physics

www.elsevier.com/locate/jcp

Computational challenges for simulations related to the NASA electric arc shock tube (EAST) experiments ☆

Dmitry V. Kotov [a,1], H.C. Yee [b,*,2], Marco Panesi [c,3], Dinesh K. Prabhu [b,4], Alan A. Wray [b,5]

[a] Center for Turbulence Research, Stanford University, Stanford, CA 94305-3035, United States
[b] NASA Ames Research Center, Moffett Field, CA 94035, United States
[c] Department of Aerospace Engineering, University of Illinois, Urbana-Champaign, IL 61801, United States

ARTICLE INFO

Article history:
Received 26 September 2013
Received in revised form 7 March 2014
Accepted 18 March 2014
Available online 26 March 2014

Keywords:
Numerical methods for problems with stiff source terms and discontinuities
Hypersonic nonequilibrium electric arc shock tube simulations
Wrong propagation speed of discontinuities
Spurious numerics
High order simulations of hypersonic viscous flows

ABSTRACT

The goal of this study is to gain some physical insights and an understanding of the computational challenges for the simulations related to the hypersonic nonequilibrium multi-species and multi-reaction experiments on the NASA Electric Arc Shock Tube (EAST). While experimental measurement does not provide any information about the radial structure of this type of flow, accurate and reliable numerical simulations can provide more insight into the physical structure of the flow to aid the design of atmospheric entry spacecrafts. The paper focuses on the spurious numerics which take place in numerical simulations of the subject physics containing stiff source terms and discontinuities. This paper is based on the knowledge gained from Yee et al. on simple reacting test cases (Yee et al. 2013, [9]) as a guide to reveal the computational challenges involved for such an extreme flow type. The results of the 1D and 2D EAST viscous and inviscid simulations using a simplified physical model are presented. The computation reveals, for the first time, that the 2D viscous model which contains both shocks and shears exhibits Tollmien–Schlichting-like instability complex patterns at the boundary layer. In addition to exhibiting spurious numerical behavior of wrong propagation speed of discontinuities by typical shock-capturing methods, there is improved understanding on the cause of numerical difficulties by previous investigators. One example is that the relative distance between the shocks and shear/contact is different from one grid spacing to another for each considered high order shock-capturing scheme. The results presented can provide insight on the numerical instability observed by previous investigations and future algorithm development for this type of extreme flow.

Published by Elsevier Inc.

☆ A revised manuscript of the 21st AIAA CFD conference paper, June 24–27, 2013, San Diego, and an expanded version of the CTR Tech Brief, "1D and 2D Simulations to the NASA Electric Arc Shock Tube Experiments" Center for Turbulence Research, Stanford University, 2012.

* Corresponding author.
E-mail addresses: dkotov@stanford.edu (D.V. Kotov), helen.m.yee@nasa.gov (H.C. Yee), mpanesi@illinois.edu (M. Panesi), dinesh.k.prabhu@nasa.gov (D.K. Prabhu), alan.a.wray@nasa.gov (A.A. Wray).
[1] Postdoctoral Fellow, Stanford Center for Turbulence Research.
[2] Senior Research Scientist, MS 258-5, NASA Ames Research Center.
[3] Assistant Professor, University of Illinois.
[4] Senior Staff Scientist, MS 229-1, NASA Ames Research Center, Associate Fellow, AIAA.
[5] Senior Research Scientist, MS 258-1, NASA Ames Research Center.

http://dx.doi.org/10.1016/j.jcp.2014.03.021
0021-9991/Published by Elsevier Inc.

1. Introduction

The Electric Arc Shock Tube (EAST) facility at NASA Ames Research Center is used to generate high-enthalpy gas tests for studying high-speed atmospheric entry physics. The shock tube consists of two sections: (1) a 10.16 cm diameter long tube (>8 m) containing the test gas mixture at the desired test pressure, and (2) a 1.3 L conical section containing the driver gas. The two sections are separated by a thin stainless steel diaphragm. The driver gas is heated by a high voltage electric arc discharge through it causing the pressure to increase to very high levels. At the high pressure generated by the discharge, the diaphragm bursts, forming a shock wave that travels at high speed through a long cylindrical tube. As the shock propagates downstream, the shock-heated gas radiates, and in a test section emission spectroscopy is used to determine the radiative signature and thereby the thermo-chemical and radiative properties of the medium.

The experiments [1,2] make use of helium as a driver gas and synthetic air ($N_2 + O_2$) as a test gas (or driven gas). The shock velocities obtained in EAST experiments range between 9 and 16 km/s. The distance between the diaphragm and the test section is 7.0 m. At the test section the spectrally and spatially resolved shock-layer radiance is analyzed by taking a snapshot of the shock wave and the following gas as they pass in front of an optical access window. It should be noted that whereas the EAST shock tube has a circular cross-section, the present simulations use 1D or 2D rectangular geometries.

It is important to note that optically probing the shocked gas does not provide any information about the radial structure of the flow in the shock tube. The experiments only provide integrated measurements that include all the absorption and emission across the tube. The experimental data obtained are useful in the verification/validation of simulation tools used in the aerothermal design of atmospheric entry spacecraft. Currently there have been very few attempts at simulating the unsteady flow in the EAST, even though simulation tools built around mathematical models incorporating the best physics can provide good insights into the nature of the flow, especially about absorption in the boundary layer that develops on the wall of the tube. Such viscous effects cannot be discerned through experiment alone.

However, there are challenges in a CFD computation of this problem. One major challenge lies in the specification of the thermochemical state of the arc-heated driver gas, i.e., the initial state. Although energy deposition into the driver gas is time dependent, the current approach has been to adjust the initial temperature until the target shock velocity is reproduced. Several other challenges arise from the need to capture accurately the spatial-temporal evolution of the flow field in order to characterize boundary layer growth on the shock tube wall. The boundary layer is the primary cause of the shock wave's deceleration, and it has important implications for re-absorption of shock layer radiation prior to instrument detection. These phenomena are unsteady and must be treated as such. For flight experiments one usually seeks a steady state solution, so that the simulation is not constrained by time accuracy requirements, and various acceleration techniques can be used. The shock tube flowfield, however, develops in time and thus requires, at a minimum, second order time integration and minimization of numerical instabilities due to the multiscale physics and stiff source terms of the flow. Similarly, the spatial relaxation scale has to be resolved accurately, and all wave interactions have to be accounted for. Initial simulations of the EAST facility have demonstrated strong sensitivity to the choice of numerical method. Therefore, schemes with high-order spatial accuracy and low dissipation are desired. The fine grid and numerical stability requirements for high speed shock-boundary layer interaction simulations is an added challenge in CFD. Furthermore, the length of the EAST facility is roughly 8 m, which translates to enormous grids. The combination of these temporal and spatial resolution requirements demands significant computer resources and simulation time to account for all important phenomena.

An additional, less well-known challenge, involves the stiffness of the source terms in the governing equations. The temperature in the shock during the experiment is above 20,000 K, which means that chemical reaction rates in the vicinity of the shock become very high and the source term describing the chemical reactions becomes stiff. As most common shock-capturing schemes have been developed for problems without source terms, when applied to problems with nonlinear and/or stiff source terms these methods can result in spurious solutions, even when solving a conservative system of equations with a conservative scheme. This kind of behavior can be observed even for a scalar case [3] as well as for the case with two species and one reaction [4]. For further information concerning this issue see the work of LeVeque and Yee, Griffiths et al., Lafon and Yee and Yee et al. [3,5–9].

For a brief introduction and earlier CFD simulations of EAST see Refs. [8,10]. Because of the asymmetric nature of the driver flow, partially due to the incomplete opening of the diaphragm and the non-symmetrical configuration of the discharge, a full 3D computation should be carried out for this problem. In the present investigation we perform less CPU-time-intensive 1D and 2D computations for the purpose of gaining first-hand understanding of the simulation challenges involved. Regarding the simulation challenges, the main focus of this study concerns the phenomena that the discontinuity locations depend on grid spacing and numerical method. For a chosen shock-capturing method, the difference in the computed discontinuity locations can be very large from one grid spacing to another for most of the standard high order methods.

The outline of this paper is as follows: In order to reveal the computational challenges for such an extreme flow related to EAST, a review of previous work done by Yee et al. [9] is given in Sections 2 and 3. Yee et al. provide with systematic analysis of spurious numerics for two simple single reaction detonation test cases. The review is to convey the spurious behavior of typical high order shock-capturing schemes. Section 2 gives a brief description of two recently developed shock-capturing methods with numerical dissipation control to minimize spurious numerics for problems containing stiff source terms [4,11–14]. The two shock-capturing methods are high order methods using the Harten subcell resolution procedure and the nonlinear filter counterparts of high order shock-capturing methods. Section 3 gives a summary of [9] on the comparison of

these low dissipative schemes with standard shock-capturing schemes in terms of spurious behavior of the numerical methods for problems with stiff source terms and discontinuities. The comparison include the performance of the Harten and Yee second-order TVD method [15,16], and standard fifth-order and seventh-order WENO schemes (WENO5 and WENO7) [17]. Although the subcell resolution idea and its filter counterparts are applicable to any high order shock-capturing method, here the study is focused on the class of WENO schemes. From here on the subcell resolution counterparts of WENO5 and WENO7 will be denoted by WENO5/SR and WENO7/SR [4]. The nonlinear filter counterparts of WENO5 and WENO7 without the subcell resolution procedure are denoted by WENO5fi & WENO7fi. If the Ducros et al. preprocessing step [18] is employed, they are denoted by, e.g., WENO5fi+split. The comparison includes the various stability and spurious behaviors found in different approaches in solving reactive governing equations, i.e. solving fully coupled system vs. fractional step procedure using the Strang splitting of the governing equations. Knowledge gained from [9] guides us to have stable simulation by employing the Strang splitting of the governing equations for a simplified flow condition that is related to the EAST experiments. Studies indicate that using the same temporal discretization, solving the fully coupled reacting flow equations with stiff source terms and discontinuities for the EAST related flow model is not stable even using a very small CFL (results not shown). These new results are presented in Section 4.

2. Overview of two recently developed high order shock-capturing schemes

Here we briefly describe two newly developed high order numerical methods with different numerical dissipation controls [4,11–14]. For simplicity of discussion only 2D reactive Euler equations are considered. It is noted that the considered schemes are applicable to 3D reactive flows. The Wang et al. [4] high order scheme with subcell resolution [4] is only developed for a single reaction case and further extension to multi-reaction cases is still under investigation. The regular WENO scheme and the Yee and Sjögreen and Sjögreen and Yee high order nonlinear filter scheme [11–14,19] are applicable to any number of species and reactions.

2.1. 2D reactive Euler equations

Consider a 2D inviscid reactive flow containing two species

$$(\rho_1)_t + (\rho_1 u)_x + (\rho_1 v)_y = K(T)\rho_2 \tag{1}$$

$$(\rho_2)_t + (\rho_2 u)_x + (\rho_2 v)_y = -K(T)\rho_2 \tag{2}$$

$$(\rho u)_t + \left(\rho u^2 + p\right)_x + (\rho uv)_y = 0 \tag{3}$$

$$(\rho v)_t + (\rho uv)_x + \left(\rho v^2 + p\right)_y = 0 \tag{4}$$

$$E_t + \left(u(E+p)\right)_x + \left(v(E+p)\right)_y = 0 \tag{5}$$

where ρ_1 is the density of burned gas, ρ_2 is the density of unburned gas, u and v are the mixture x- and y-velocities, E is the mixture total energy per unit volume, p is the pressure, $K(T)$ is the chemical reaction rate and T is the temperature. The pressure is given by

$$p = (\gamma - 1)\left(E - \frac{1}{2}\rho\left(u^2 + v^2\right) - q_0\rho_2\right), \tag{6}$$

where the temperature $T = p/\rho$ and q_0 is the chemical heat released in the reaction.

The mass fraction of the unburned gas is $z = \rho_2/\rho$. The mixture density is $\rho = \rho_1 + \rho_2$.

The reaction rate $K(T)$ is modeled e.g. by an Arrhenius law

$$K(T) = K_0 \exp\left(\frac{-T_{ign}}{T}\right), \tag{7}$$

where K_0 is the reaction rate constant and T_{ign} is the ignition temperature.

2.2. High order finite difference methods with subcell resolution for advection equations with stiff source terms

The general fractional step approach based on Strang-splitting [20] for the 2D reactive Euler equations written in vector notation is as follows:

$$U_t + F(U)_x + G(U)_y = S(U) \tag{8}$$

The numerical solution U^{n+1} at time level t_{n+1} is approximated by

$$U^{n+1} = A\left(\frac{\Delta t}{2}\right) R(\Delta t) A\left(\frac{\Delta t}{2}\right) U^n. \tag{9}$$

Here, U is the conservative variable vector, and F and G are the convection fluxes in the x and y directions, respectively. S is the source term vector. The reaction operator R is over a time step Δt and the convection operator A is over $\Delta t/2$. The two half-step reaction operations over adjacent time steps can be combined to save cost. In order to obtain more accurate results in the reaction zone we can consider the reaction step that consists of N_r sub steps of the reaction difference operator, i.e.,

$$U^{n+1} = A\left(\frac{\Delta t}{2}\right) R\left(\frac{\Delta t}{N_r}\right) \cdots R\left(\frac{\Delta t}{N_r}\right) A\left(\frac{\Delta t}{2}\right) U^n \tag{10}$$

Any high order shock-capturing scheme can be used for the convection operator. The convection operator A is defined to approximate the solution of the homogeneous part of the problem on the time interval, i.e.,

$$U_t + F(U)_x + G(U)_y = 0, \quad t_n \leqslant t \leqslant t_{n+1}. \tag{11}$$

The reaction operator R is defined to approximate the solution on a time step of the reaction problem:

$$\frac{dU}{dt} = S(U), \quad t_n \leqslant t \leqslant t_{n+1}. \tag{12}$$

In case of viscous flows, the corresponding viscous flux derivatives should be added to (11).

For the majority of the numerical experiments, the original Jiang–Shu 5th-order WENO (WENO5) using the Roe flux and RK4 (4th-order Runge–Kutta) time discretization is used for the convection operator. If there is no smearing of discontinuities in the convection step, any ordinary differential equation (ODE) solver can be used as the reaction operator. However, all the standard shock-capturing schemes will produce a few transition points in the shock when solving the convection equation. These transition points are usually responsible for causing incorrect numerical results in the stiff case. Thus, a direct application of a standard ODE solver at these transition points will result in incorrect shock speed. To avoid this, here the Harten subcell resolution technique [21] is employed before calling the ODE solver. If $N_r > 1$, the subcell resolution technique is performed at every N_r sub-iteration step.

2.3. Well-balanced high order filter schemes for reacting flows [11–14,19]

The high order nonlinear filter scheme of Yee et al. [11,12,19], if used in conjunction with a dissipative portion of a well-balanced shock-capturing scheme as the nonlinear numerical flux, is a well-balanced scheme [14]. The well-balanced high order nonlinear filter scheme for reacting flows, when used to solve the fully coupled system (8), consists of three steps.

2.3.1. Preprocessing step

Before the application of a high order non-dissipative spatial base scheme, a preprocessing step is employed to improve the stability. The inviscid flux derivatives of the governing equation(s) are split in the following three ways, depending on the flow types and the desire for rigorous mathematical analysis or physical argument.

- Entropy splitting of Olsson and Oliger [22] and Yee et al. [23,24]. The resulting form is non-conservative and the derivation is based on entropy norm stability with boundary closure for the initial value boundary problem.
- The system form of the Ducros et al. splitting [18]. This is a conservative splitting and the derivation is based on physical arguments.
- Tadmor entropy conservation formulation for systems [25]. The derivation is based on mathematical analysis. It is a generalization of Tadmor's entropy formulation to systems and has not been fully tested on complex flows.

See Honein [26] for a comparison of the entropy splitting and other earlier momentum conservation methods. It is noted that the splitting of the governing equations to an equivalent form as the preprocessing step is not to be confused with the Strang splitting procedure in solving the reactive equations.

2.3.2. Base scheme step

A full time step is advanced using a high order non-dissipative (or very low dissipation) spatially central scheme on the split form of the governing partial differential equations (PDEs). Summation-by-parts (SBP) boundary operator [27,28] and matching order conservative high order free stream metric evaluation for curvilinear grids [29] are used. High order temporal discretization such as the third-order or fourth-order Runge–Kutta (RK3 or RK4) method is used. It is remarked that other temporal discretizations can be used for the base scheme step.

2.3.3. Post-processing (nonlinear filter step)

After the application of a non-dissipative high order spatial base scheme on the split form of the governing equation(s), to further improve nonlinear stability from the non-dissipative spatial base scheme, the post-processing step of Refs. [11, 12,19] is used to nonlinearly filter the solution by a dissipative portion of a high order shock-capturing scheme with a local flow sensor. The flow sensor provides locations and amounts of built-in shock-capturing dissipation that can be further

reduced or eliminated. The idea of these nonlinear filter schemes for turbulence with shocks is that, instead of solely relying on very high order high-resolution shock-capturing methods for accuracy, the filter schemes [12,19,23,30,31] take advantage of the effectiveness of the nonlinear dissipation contained in good shock-capturing schemes as stabilizing mechanisms (a post-processing step) at locations where needed. At each grid point, a local flow sensor, e.g., a multi-resolution wavelet, would be employed to analyze the regularity of the computed flow data. Only the discontinuity locations would receive the full amount of shock-capturing dissipation. In smooth regions no shock-capturing dissipation would be added. In regions with strong turbulence a small fraction of the shock-capturing dissipation would be added to improve stability. The nonlinear dissipative portion of a high-resolution shock-capturing scheme can be any shock-capturing scheme. For reacting flow it is best to employ the dissipative portion of a well-balanced shock-capturing scheme.

Some attributes of the high order filter schemes are:

- Spatial Base Scheme: High order and conservative (no flux limiter or Riemann solver)
- Physical Viscosity: Contribution of physical viscosity, if it exists, is automatically taken into consideration by the base scheme in order to minimize the amount of numerical dissipation to be used by the filter step
- Efficiency: One Riemann solve per dimension per time step, independent of time discretizations (less CPU time and fewer grid points than their standard shock-capturing scheme counterparts)
- Accuracy: Containment of numerical dissipation via a local wavelet flow sensor
- Well-balanced scheme: These nonlinear filter schemes are well-balanced schemes for certain chemical reacting flows [14]
- Stiff Combustion with Discontinuities: For some stiff reacting flow test cases, it appears that the high order filter scheme is able to obtain the correct propagation speed of discontinuities on coarse, underresolved meshes for which the standard high order shock-capturing (e.g., WENO) schemes cannot (see the results in the next section)
- Parallel Algorithm: Suitable for most current supercomputer architectures

The nonlinear filter counterpart of the subcell resolution method employing, e.g., WENO5 or WENO7 as the dissipative portion of the filter numerical flux (WENO5fi or WENO7fi) can be obtained in a similar manner with the nonlinear filter scheme used for the convection operator and will be denoted by WENO5fi/SR or WENO7fi/SR.

3. Spurious behavior of numerical schemes

To make the paper more self-contained, this section reviews the recent work of Yee et al. [9]. Before showing the effects of the spurious numerics encountered in the EAST simulations, we first illustrate the commonly occurring and yet not well known phenomenon in practical CFD of the wrong propagation speed of discontinuities on coarse grids for problems with stiff source terms reported. Yee et al. [9] and references cited therein show that the degree of error in the propagation speed of discontinuities is highly dependent on the amount of numerical dissipation and accuracy of the numerical method. The manner in which the smearing of discontinuities is contained by the numerical method and the overall amount of numerical dissipation being employed plays a major role. Depending on the numerical method, time step and grid spacing, the numerical simulation may lead to (a) the correct solution (within the truncation error of the scheme), (b) a divergent solution, (c) a wrong propagation speed of discontinuities or (d) other spurious solutions that are solutions of the discretized counterparts but are not solutions of the governing equations. The test case is the Arrhenius case considered in several papers (see Refs. [4,9,32–34]). The initial values consist of totally burned gas on the left-hand side and totally unburned gas on the right-hand side. The dimensionless density, velocity, and pressure of the unburned gas are given by $\rho_u = 1$, $u_u = 0$ and $p_u = 1$.

The initial state of the burned gas is calculated from the Chapman–Jouguet (C–J) condition:

$$p_b = -b + \left(b^2 - c\right)^{1/2}, \tag{13}$$

$$\rho_b = \frac{\rho_u[p_b(\gamma+1) - p_u]}{\gamma p_b}, \tag{14}$$

$$S_{CJ} = \left[\rho_u u_u + (\gamma p_b \rho_b)^{1/2}\right]/\rho_u, \tag{15}$$

$$u_b = S_{CJ} - (\gamma p_b/\rho_b)^{1/2}, \tag{16}$$

where

$$b = -p_u - \rho_u q_0(\gamma - 1), \tag{17}$$

$$c = p_u^2 + 2(\gamma - 1)p_u \rho_u q_0/(\gamma + 1). \tag{18}$$

The heat release $q_0 = 25$ and the ratio of specific heats is set to $\gamma = 1.4$. The ignition temperature $T_{ign} = 25$ and $K_0 = 16{,}418$. The computation domain is $[0, 30]$. Initially, the discontinuity is located at $x = 10$. At time $t = 1.8$, the detonation wave has moved to $x = 22.8$. The reference solution is computed by the regular WENO5 scheme with 10,000 uniform grid points and $CFL = 0.05$.

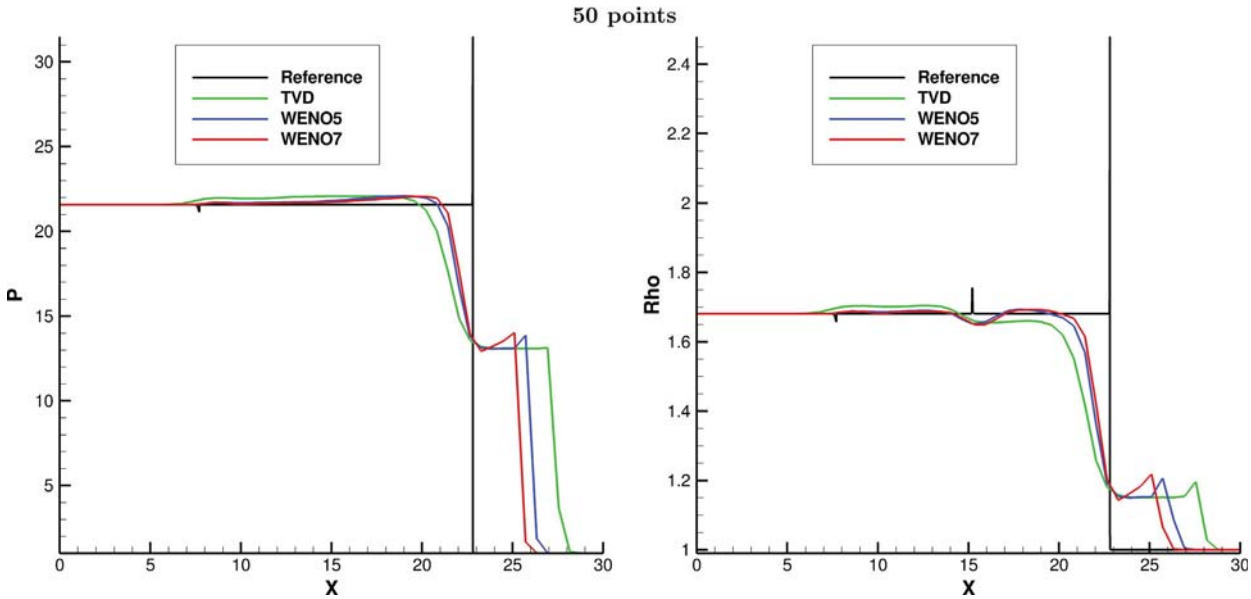

Fig. 1. 1D C–J detonation problem, Arrhenius case for the original stiffness K_0 at $t = 1.8$: Pressure and density comparison among three standard shock-capturing methods (TVD, WENO5, WENO7) using 50 uniform grid points with $CFL = 0.05$.

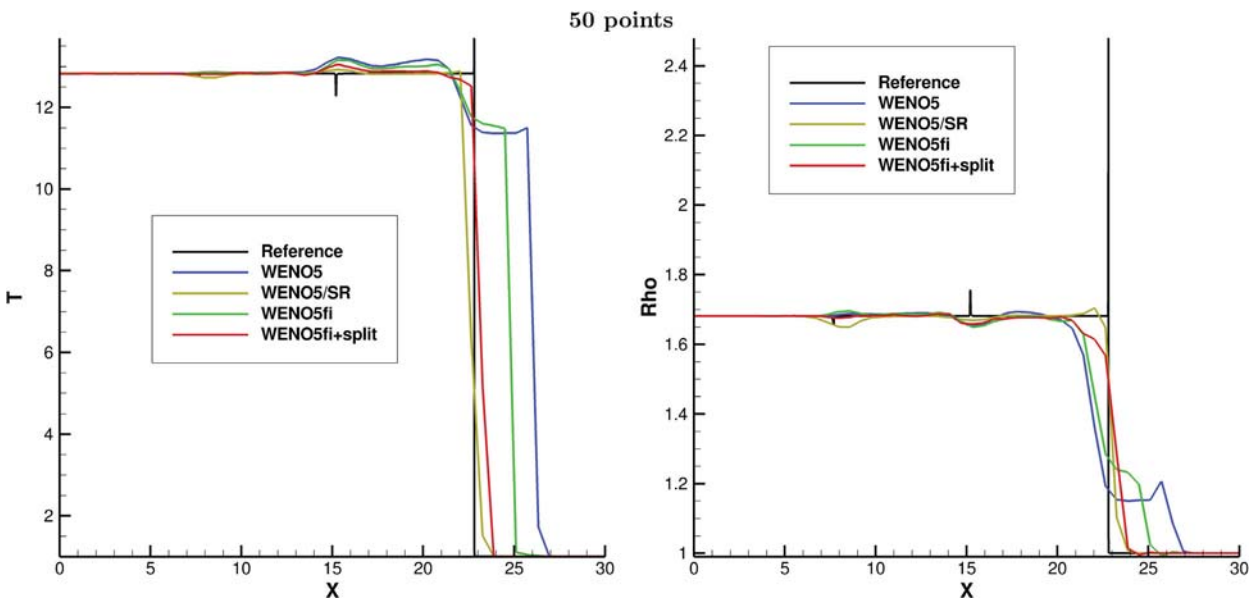

Fig. 2. 1D C–J detonation problem, Arrhenius case for the original stiffness K_0 at $t = 1.8$: Temperature and density comparison among standard high order shock-capturing methods and low dissipative methods (WENO5, WENO5/SR, WENO5fi+split and WENO5fi/SR+split) using 50 uniform grid points with $CFL = 0.05$.

3.1. Initial study of scheme behavior [35]

Fig. 1 shows the pressure and density comparison among the standard TVD, WENO5 and WENO7 using 50 uniform grid points and $CFL = 0.05$ for the same stiffness $K_0 = 16{,}418$ used in Yee et al. [35]. Fig. 2 shows the pressure and density comparison among the standard WENO5 scheme, WENO5/SR, WENO5fi and WENO5fi+split using 50 uniform grid points. For this particular problem and grid size, all standard TVD WENO5 and WENO7 exhibit wrong shock speed of propagation with the lower order and more dissipative schemes exhibiting the largest error. WENO5fi+split compares well with WENO5/SR for the computed pressure solution. WENO5/SR and WENO5fi+split can capture the correct structure using fewer grid points than those in Helzel et al. [33] and Tosatto and Vigevano [34]. It is remarked that with such a coarse grid it is not possible to resolve the detonation front within one to several grid cells. Here we are only concerned with the correct speed of discontinuities propagation using a very coarse grid.

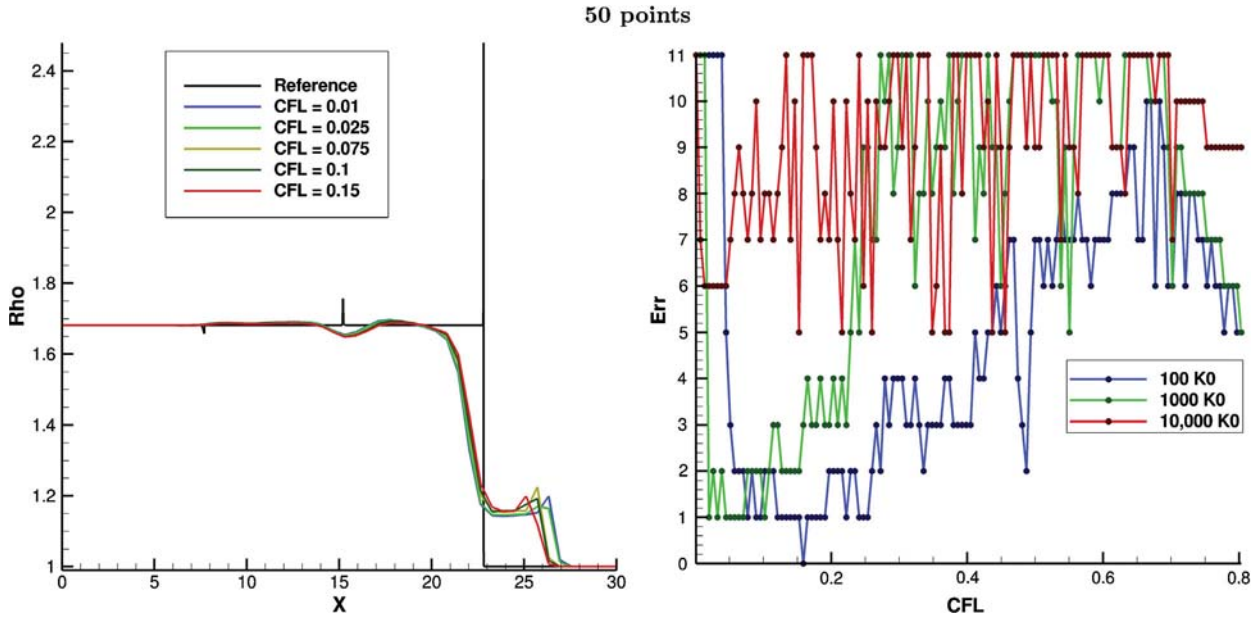

Fig. 3. 1D C–J detonation problem, Arrhenius case using 50 uniform grid points: Density comparison for seven CFL numbers using WENO5 (left). Number of grid points away from the reference solution (Err) as a function of the CFL number (128 CFL values with $6.316455696 \times 10^{-3}$ equal increment) for three stiffness coefficients $100K_0, 1000K_0, 10{,}000K_0$ using WENO5. All the CFL values for the inviscid simulations are based on the convection part of the PDEs.

3.2. Scheme behavior as a function of CFL, grid refinement and stiffness of the source terms

A systematic study of the spurious numerics for the same test case has been performed in Refs. [4,9,32]. Here, a summary of results reported in the aforementioned publications is described. Fig. 3 shows the effect of the time steps for five CFL values that are under the CFL limit (left subfigure), using 50 grid points and WENO5. The right subfigure shows the error in terms of the number of grid points away from the reference shock location (Err) for three stiffness coefficients $K_0, 100K_0$ and $1000K_0$ as the function of 128 discrete CFL values. The 128 discrete CFL values are $(0.0001 \leqslant CFL \leqslant 0.803)$ with $6.316455696 \times 10^{-3}$ equal increment. Here, Err is rounded down to the nearest integer number. Note that the CFL limit for WENO5/SR and its filter counterparts are lower than 0.8 due to the explicit Euler reaction step. For all plots related to this study, a negative "Err" value indicates the number of grid points behind the reference shock position. For certain values of CFL divergent solutions might occur that are outside the plotting area. All the CFL values for the inviscid simulations are based on the convection part of the PDEs. Fig. 4 illustrates the error for 128 discrete CFL values for the three improved high order shock-capturing schemes (WENO5/SR, WENO5fi+split and WENO5fi/SR+split). The study is for three uniform grids 50, 150 and 300 (left to right columns in the plot) and the three stiffness coefficients $K_0, 100K_0$ and $1000K_0$ (top to bottom in the plot). As the stiffness coefficient increases, it is more and more difficult to obtain the correct shock locations using WENO5/SR.

3.3. Solving fully coupled reactive equations vs. Strang Splitting of the reactive equations

All of the above computations (including the EAST computation to be shown) are performed by solving the reactive equations via the Strang splitting procedure. Comparison of the solution behavior between solving the fully coupled reactive equations (without the Strang Splitting procedure) and the Strang Splitting procedure is reported in Kotov et al. [32]. Studies show that solving the fully coupled reactive equations is very unstable for standard shock-capturing schemes as well as for their high order filter counterparts. Using a very small CFL for K_0, and the same three grids and CFL range, a similar wrong propagation speed of discontinuities is observed by standard shock-capturing schemes for all considered CFL. However, WENO5fi+split and WENO7fi+split are able to obtain the correct shock speed using the same small CFL (with the exception of the one grid point error for WENO7fi+split using 300 grid). For stiffness coefficients $100K_0$ and $1000K_0$ using the same three grids, no stable solutions are obtained except in the case of $100K_0$ and 300 grid points using $CFL = 6.316455696 \times 10^{-3}$ (in which case a wrong speed solution is obtained). See Fig. 5 for the K_0 result. To further examine the difference between the two procedures in solving the reactive equations, we compare the fully coupled solution procedure with the Strang splitting procedure using 10,000 grid points. For fine enough grid resolution, both procedures produce the same result. WENO5/SR is not present on the figure as it requires Strang splitting.

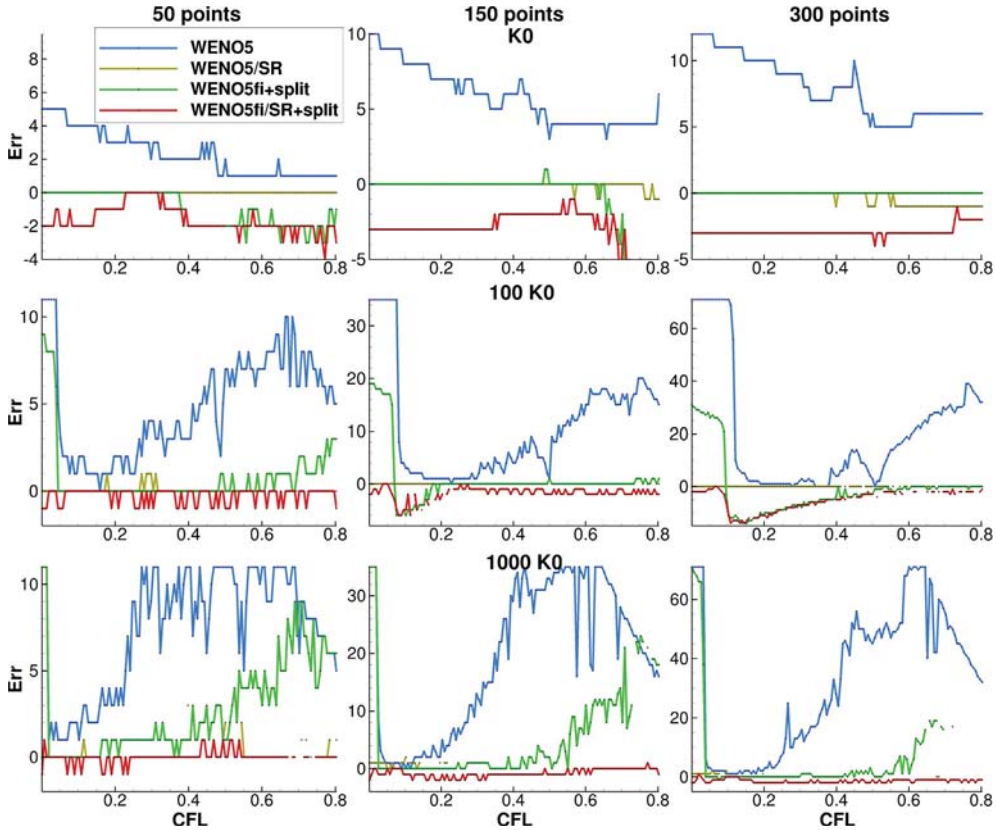

Fig. 4. 1D C–J detonation problem, Arrhenius case at $t = 1.8$: Number of grid points away from the reference shock position (Err) as a function of the CFL number (128 discrete CFL values with $6.316455696 \times 10^{-3}$ equal increment) for three low dissipative shock-capturing methods using $50, 150, 300$ uniform grid points (across) and for stiffness $K_0, 100K_0, 1000K_0$ (top to bottom). See Fig. 3 for additional information.

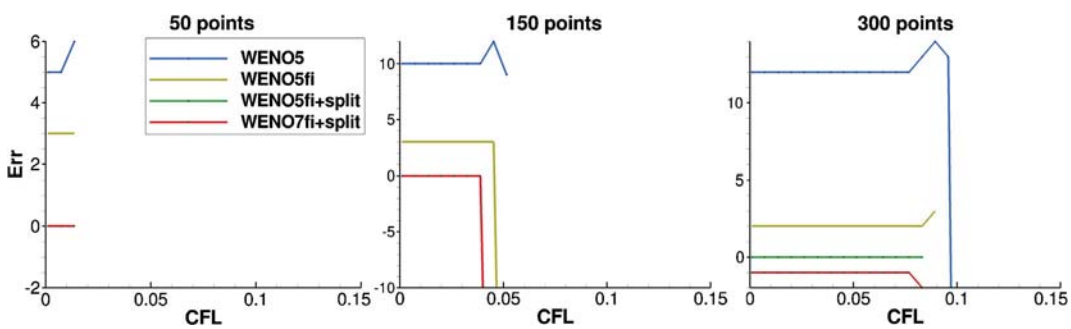

Fig. 5. No Strang splitting results for the 1D C–J detonation problem, Arrhenius case at $t = 1.8$: Number of grid points away from the reference shock position (Err) as a function of the CFL number (128 discrete CFL values with $6.316455696 \times 10^{-3}$ equal increment) for three low dissipative shock-capturing methods using $50, 150, 300$ uniform grid points (across) and for stiffness K_0.

3.4. Effect of employing a cut-off safeguard procedure

All of the results presented employ a cut-off safeguard procedure if densities are outside the permissible range. Fig. 6 shows the same computation without the cut-off safeguard procedure using the Strang splitting. The procedure is also very unstable. For K_0, and the same three grids and CFL range, a similar wrong propagation speed of discontinuities is observed by WENO5 for small CFL. However, WENO5/SR and WENO5fi+split are able to obtain the correct shock speed using the same small CFL. WENO5fi/SR+split is not able to obtain the correct shock speed for even the smallest considered CFL value ($CFL = 6.316455696 \times 10^{-3}$). One of the possible causes might be due to the incompatibility of the combined Strang splitting using $N_r = 2$, and the nonlinear filter procedure. For stiffness coefficients $100K_0$ and $1000K_0$ using the same three grids, no stable solutions are obtained except in the case of $100K_0$ and 300 grid points using $CFL = 6.316455696 \times 10^{-3}$ (a wrong speed solution is obtained). See Fig. 6 for the K_0 result. The solution behavior of solving the

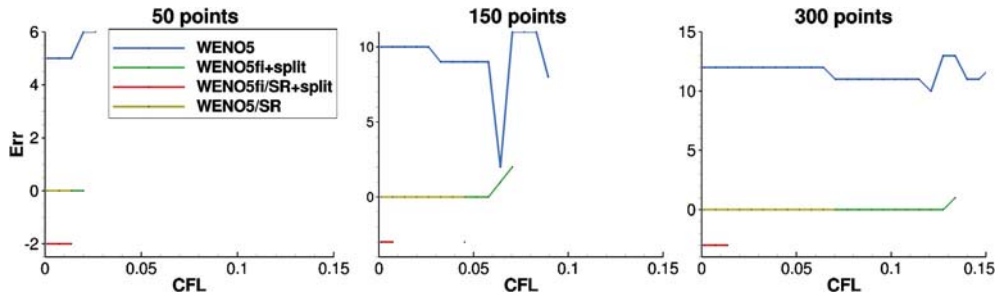

Fig. 6. No cutoff safeguard procedure and Strang splitting results for the 1D C–J detonation problem, Arrhenius case at $t = 1.8$: Number of grid points away from the reference shock position (Err) as a function of the CFL number (128 discrete CFL values with $6.316455696 \times 10^{-3}$ equal increment) for three low dissipative shock-capturing methods using 50, 150, 300 uniform grid points (across) and for stiffness K_0.

fully coupled reactive equations is similar to using the Strang splitting without the cut-off safeguard procedure. Studies of Kotov et al. [32] also indicate that there is no visible difference in solution behavior in using the cut-off safeguard procedure or not when solving the fully coupled reactive equations.

Most often, under an extreme flow condition, a positivity preserving version of WENO5 might help improve accuracy and spurious numerics, see [36] for a study. For this particular problem positivity preserving WENO5 provides only a minimal improvement.

4. EAST related computations

In this section we will give the formulation of the problem related to EAST and give some details of the numerical simulations. Then we will discuss the results of the 1D and 2D computations and compare the results obtained by several standard shock-capturing methods and their filter counterpart schemes [11,19] for the early time evolution of the flow. Note that for this viscous simulation all the CFL values are based on the convection and viscous parts of the PDEs.

4.1. Governing equations

Consider the 3D reactive Navier–Stokes equations for a one-temperature energy model:

$$\frac{\partial \rho_s}{\partial t} + \frac{\partial}{\partial x_j}(\rho_s u_j + \rho_s d_{sj}) = \Omega_s \tag{19}$$

$$\frac{\partial}{\partial t}(\rho u_i) + \frac{\partial}{\partial x_j}(\rho u_i u_j + p\delta_{ij} - \tau_{ij}) = 0 \tag{20}$$

$$\frac{\partial}{\partial t}(\rho E) + \frac{\partial}{\partial x_j}\left(u_j(\rho E + p) + q_j + \sum_s \rho_s d_{sj} h_s - u_i \tau_{ij}\right) = 0, \tag{21}$$

where $i = 1, 2, 3$, $(\rho_s, \rho u_i, \rho E)$ are the conserved variables and ρ_s are the partial densities with $k = 1, \ldots, N_s$ for a mixture of N_s species. The mixture total density, the pressure, and the total energy per unit volume are

$$\rho = \sum_s \rho_s, \qquad p = RT \sum_{s=1}^{N_s} \frac{\rho_s}{M_s}, \qquad \rho E = \sum_{s=1}^{N_s} \rho_s \left(e_s(T) + h_s^0\right) + \frac{1}{2}\rho v^2, \tag{22}$$

where R is the universal gas constant, h_s^0 are the species formation enthalpies, and M_s are the species molar masses. The viscous stress tensor is

$$\tau_{ij} = \mu\left(\frac{\partial u_i}{\partial x_j} + \frac{\partial u_j}{\partial x_i}\right) - \mu\frac{2}{3}\frac{\partial u_k}{\partial x_k}\delta_{ij}. \tag{23}$$

The diffusion flux is

$$d_{sj} = -D_s \frac{\partial X_s}{\partial x_j}, \tag{24}$$

where D_s is the diffusion coefficient and X_s is the mole fraction of species s. The conductive heat flux is

$$q_j = -\lambda \frac{\partial T}{\partial x_j}, \tag{25}$$

where λ is the thermal conductivity of the mixture. The chemical source term is

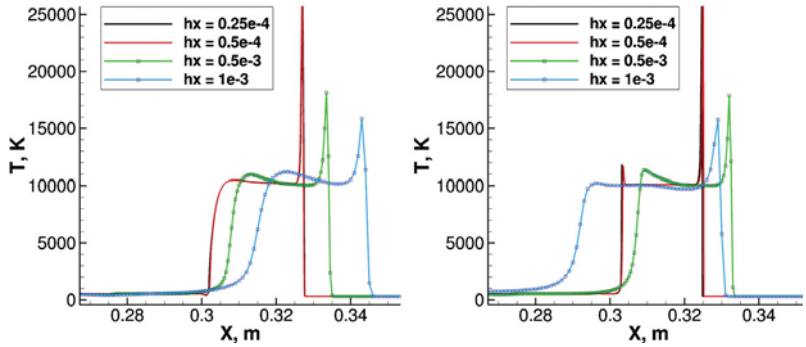

Fig. 7. Viscous and inviscid comparison of the 1D, 13 species EAST problem: Second-order Harten–Yee TVD simulation for four levels of grid refinement with $CFL = 0.8$ and $t_{end} = 3.25 \times 10^{-5}$ s. The Δx grid size is: 10^{-3} m, 5×10^{-4} m, 5×10^{-5} m, 2.5×10^{-5} m. Left: viscous case, right: inviscid case.

$$\Omega_s = M_s \sum_{r=1}^{N_r} (b_{s,r} - a_{s,r}) \left[k_{f,r} \prod_{m=1}^{N_s} \left(\frac{\rho_m}{M_m} \right)^{a_{m,r}} - k_{b,r} \prod_{m=1}^{N_s} \left(\frac{\rho_m}{M_m} \right)^{b_{m,r}} \right], \tag{26}$$

where a and b are the stoichiometric coefficients, and the forward reaction rate coefficients, k_{fr}, are given by Arrhenius' law:

$$k_{fr} = A_{f,r} T^{n_{f,r}} \exp(-E_{f,r}/kT). \tag{27}$$

The backward reaction rate coefficients are computed as $k_{b,r} = k_{f,r}/K_{c,r}^{eq}$, where $K_{c,r}^{eq}$, is the equilibrium constant. The details of formulation for the particular 1D and 2D EAST problems will be given in the sections below.

4.2. Numerical simulation

All the computations employ the multi-dimensional high order single/overset grid nonequilibrium code ADPDIS3D [37,38]. 1D and 2D simplifications of the 3D EAST problem are considered using a single block option in the code. In addition, a one-temperature model is used, though the two-temperature model is required in order to obtain better agreement with the experiments. For the 2D case axisymmetric geometry is not used as this option has not been implemented into ADPDIS3D; planar geometry is used instead. The MUTATION library [39,40], developed by Thierry Magin and Marco Panesi, is used to provide reaction rates and transport properties.

All the results are obtained using the fractional step approach employing the Strang splitting [20] of the reactive governing equation. The integration of the convection equations is performed using the Runge–Kutta (RK) method of the appropriate order, i.e. second-order (RK2) for TVD and fourth-order (RK4) for high-order WENO. For the integration of the source terms first the analysis of the chemical rates for each grid point is performed. If the rates are low so that the resulting ODE is not stiff, simple explicit Euler or first-order RK (RK1) is used. For the integration of the ODE in a stiff case the DLSODE routine from the ODEPACK [41] package is used.

As the stiff reactions for the EAST problem take place mostly in the shock zone, the number of points with stiff reactions is relatively small, and they are mostly concentrated in a relatively small geometrical region. This result in a loss of efficiency when computing the problem using multiple processors. In order to increase the efficiency of the multiprocessing computations, all points with stiff chemical reactions are treated separately. All the local data of each point needed for solving the stiff ODE are uniformly redistributed among all the processors. Then each processor solves stiff ODE using ODEPACK and the result is distributed back to the processor of origin. The list of points with stiff ODE is updated dynamically as the shock propagates. This algorithm was found to significantly increase the performance of the multiprocessing computations for the EAST problem.

4.3. 1D EAST simulations

The computational domain has a total length of 8.5 m. At the initial time the left side of the domain with length 0.1 m is a high pressure region. The right side of the domain, with length 8.4 m is a low pressure region. Since the temperature in the vicinity of the shock can reach more than 20,000 K, ionized species must be taken into account. Here we consider the gas mixture as consisting of 13 species: e^-, He, N, O, N_2, NO, O_2, N_2^+, NO^+, N^+, O_+^2, O^+, and He^+. The reaction mechanism consists of 25 reactions with the Arrhenius law (27) rate parameters given in Table 1.

The initial conditions of the high and low pressure regions are listed in Table 2. The initial driver gas temperature is taken to be 6000 K, as in McCorkle and Hassan [10], and the pressure $p = 12.7116$ MPa is chosen to obtain a shock velocity of approximately 10 km/s in our computation, which is a typical velocity observed in the experiment. For the left-side boundary an Euler (slip) wall condition is applied, and for the right-side a zero gradient condition is applied for all variables.

Table 1
Reaction rate parameters according to Arrhenius law (27).

Reaction	$A_{f,r}$, mole m^{-3}/s	$n_{f,r}$	$E_{f,r}$, K	Comment
$N + e^- = N^+ + 2e^-$	2.50E+034	−3.82	168,600	
$O + e^- = O^+ + 2e^-$	3.90E+033	−3.78	158,500	
$O + N = NO^+ + e^-$	8.80E+008	1	31,900	
$N_2 + M = 2N + M$	3.00E+022	−1.6	113,200	$M = N, O, N^+, O^+$
$N_2 + M = 2N + M$	7.00E+021	−1.6	113,200	$M = N_2, NO, O_2, N_2^+, O_2^+, NO^+$
$N_2 + M = 2N + M$	1.20E+025	−1.6	113,200	$M = e^-$
$O_2 + M = 2O + M$	1.00E+022	−1.5	59,500	$M = N, O, N^+, O^+$
$O_2 + M = 2O + M$	2.00E+021	−1.5	59,500	$M = N_2, NO, O_2, N_2^+, O_2^+, NO^+$
$NO + M = N + O + M$	1.10E+017	0	75,500	$M = N, O, N^+, O^+$
$NO + M = N + O + M$	5.00E+015	0	75,500	$M = N_2, NO, O_2, N_2^+, O_2^+, NO^+$
$NO + O = O_2 + N$	8.40E+012	0	19,450	
$N_2 + O = NO + N$	6.40E+017	−1	38,400	
$O + O = O_2^+ + e^-$	7.10E+002	2.7	80,600	
$N + N = N_2^+ + e^-$	4.40E+007	1.5	67,500	
$O + NO^+ = N^+ + O_2$	1.00E+012	0.5	77,200	
$N_2 + N^+ = N + N_2^+$	1.00E+012	0.5	12,200	
$N + O_2^+ = O_2 + N^+$	8.70E+013	0.14	28,600	
$NO + O^+ = O_2 + N^+$	1.40E+005	1.9	26,600	
$N_2 + O_2^+ = O_2 + N_2^+$	9.90E+012	0	40,700	
$O + O_2^+ = O_2 + O^+$	4.00E+012	−0.09	18,000	
$N + NO^+ = O^+ + N_2$	3.40E+013	−1.08	12,800	
$NO^+ + O_2 = O_2^+ + NO$	2.40E+013	0.41	32,600	
$NO^+ + O = O_2^+ + N$	7.20E+012	0.29	48,600	
$O^+ + N_2 = N_2^+ + O$	9.10E+011	0.36	22,800	
$NO^+ + N = N_2^+ + O$	7.20E+013	0	35,500	

Table 2
High (left) and low (right) pressure region initial data

ρ	1.10546 kg/m^3	ρ	3.0964×10^{-4} kg/m^3
T	6000 K	T	300 K
p	12.7116 MPa	p	26.771 Pa
Y_{He}	0.9856	Y_{O_2}	0.21
Y_{N_2}	0.0144	Y_{N_2}	0.79

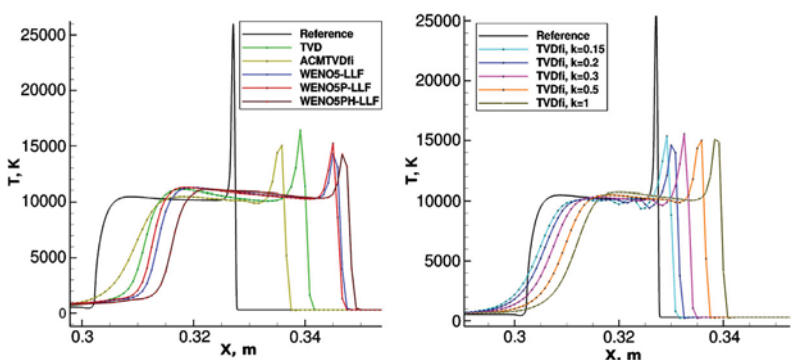

Fig. 8. 1D, 13 species EAST problem: Comparison among methods using 601 point grids with $CFL = 0.6$ and $t_{end} = 3.25 \times 10^{-5}$ s. Left subfigure: Reference solution (TVD on a 10,001 point grid), TVD, ACMTVDfi using $\kappa = 0.5$, WENO5-llf, WENO5P-llf, WENOPH-llf. Right: ACMTVDfi using $\kappa = 1, 0.5, 0.3, 0.2, 0.15$. See text for method notation.

Uniform 1-D grids are used for these simulations. To save computational cost, an initial computational domain of $(-0.1, 0.4)$ m is generated. During the computation the shock location is calculated at each time step. When the shock is close enough to the right boundary, the computational domain is increased on the downstream side by 0.5 m.

Fig. 7 shows a four level grid refinement study comparing the difference between the viscous and inviscid computations. The left subfigure of Fig. 7 shows the viscous case computation using the Harten–Yee second-order TVD scheme [15,16] for four grids with $\Delta x = 10^{-3}$ m, 5×10^{-4} m, 5×10^{-5} m and 2.5×10^{-5} m at time $t_{end} = 0.325 \times 10^{-4}$ s. One can observe

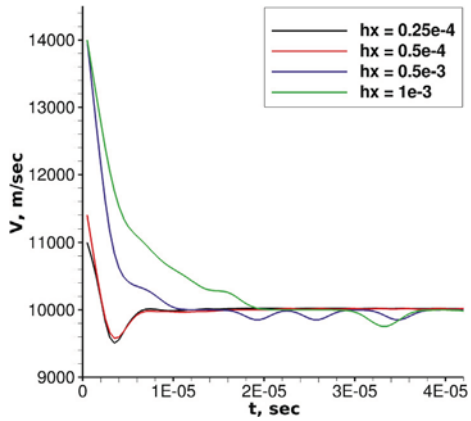

Fig. 9. 1D, 13 species EAST problem: shock velocity time dependance solution using $\Delta t = 5 \times 10^{-7}$ s on four Δx: 10^{-3} m, 5×10^{-4} m, 5×10^{-5} m, 2.5×10^{-5} m.

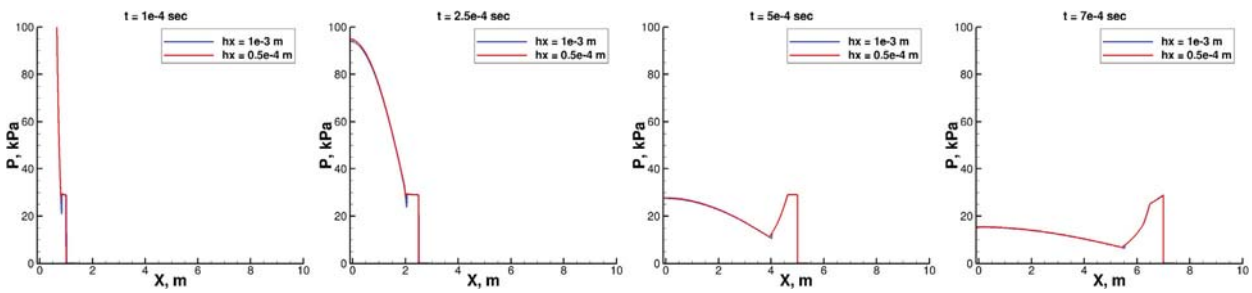

Fig. 10. 1D, 13 species EAST problem: pressure evolution during full shock tube length calculation on two grids with $\Delta x = 10^{-3}$ m and 5×10^{-4} m. Snapshots for $t = 1 \times 10^{-4}$ s, 2.5×10^{-4} s, 5×10^{-4} s and 7×10^{-4} s.

a significant shift in the shear (left discontinuity) and the shock (right discontinuity) locations as the grid is refined. The distance between the shear and the shock shrinks as the grid is refined. The difference between shock locations obtained on the grids with $\Delta x = 5 \times 10^{-5}$ m and 2.5×10^{-5} m is less than 0.3%. Thus the solution using $\Delta x = 5 \times 10^{-5}$ m can be considered as the reference solution. The right subfigure of Fig. 7 shows the same study using the same scheme for the inviscid case. In this case the convergence to the reference solution occurs a little slower and in a nonlinear way.

The left subfigure of Fig. 8 shows a comparison among five methods obtained on a coarse grid ($\Delta x = 10^{-3}$ m) with the reference solution. The scheme labels are defined as follows:

- ACMTVDfi: Second-order central base scheme using ACM flow sensor. See Yee et al. [30] for further information on filter schemes
- WENO5-llf: Fifth-order WENO (WENO5) using the local Lax–Friedrichs flux
- WENO5P-llf: Positive WENO5 of Zhang and Shu [42] using the local Lax–Friedrichs flux
- WENO5PH-llf: Positive WENO5 of Hu et al. [43] using the local Lax–Friedrichs flux

The right subfigure of Fig. 8 shows a comparison of ACMTVDfi using a different weight parameter κ of the ACM flow sensor. The smaller the κ, the smaller the amount of TVD dissipation that is used. Among the considered schemes, Fig. 8 indicates that the least dissipative scheme predicts the shear and shock locations best when compared with the reference solution. The results indicate that ACMTVDfi is slightly more accurate than WENO5-llf. This is due to the fact that ACMTVDfi reduces the amount of numerical dissipation away from high gradient regions. Using the subcell resolution method of Wang et al. [4] by applying it to only one of the reactions in this multireaction flow does not improve the performance over standard schemes.

Fig. 9 shows the shock velocity time dependence obtained on the four levels of grid refinement with $\Delta x = 10^{-3}$ m, 5×10^{-4} m, 5×10^{-5} m, and 2.5×10^{-5} m. The shock velocity is computed by taking a numerical derivative of the shock location as a function of time with some smoothing. During the first 5×10^{-6} s the computed velocity has a strong dependence on the grid. After this initial duration the computed velocities on the four grids asymptotically approach the same level. The result suggests that the major contribution to the error in shock location obtained on the coarse grid is due to the first 5×10^{-6} s. A similar behavior has been observed by other authors; see e.g., Refs. [44,45] for the perfect gas case.

Figs. 10 and 11 show time evolution of pressure during full shock tube length calculation on two grids with $\Delta x = 10^{-3}$ m and 5×10^{-4} m. With respect to the scale of the figure the difference between shock location obtained on these two grids

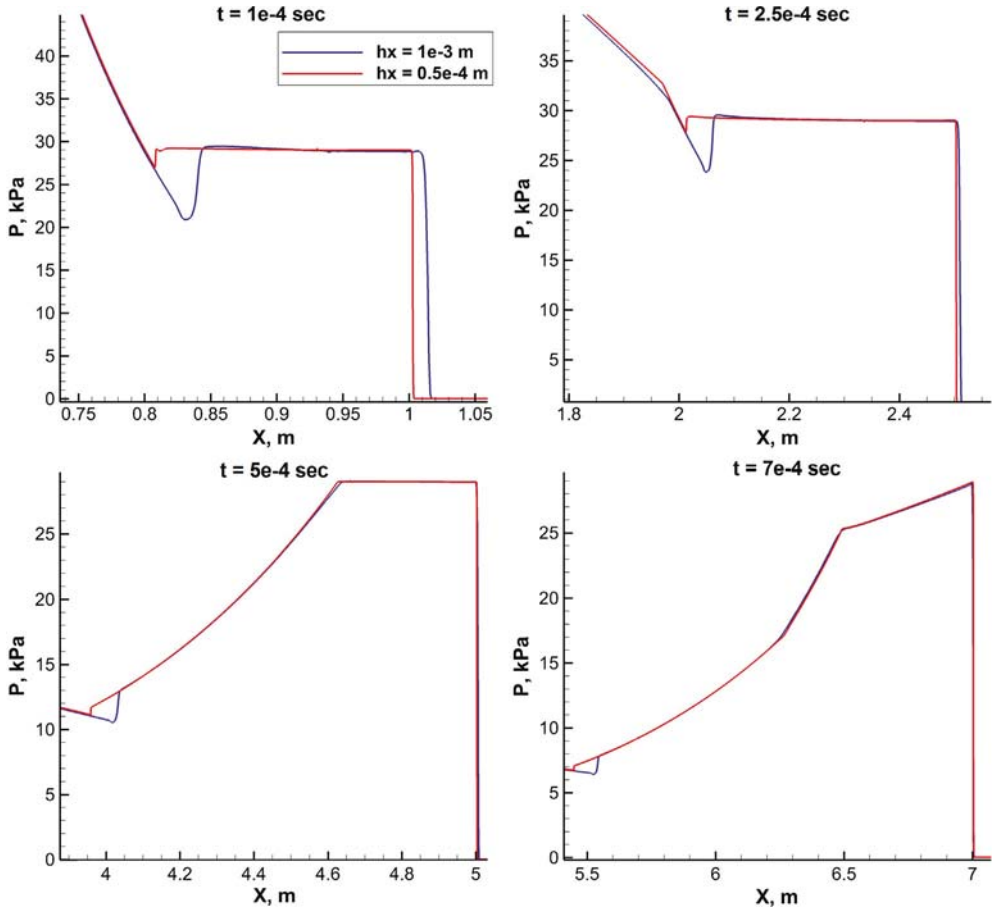

Fig. 11. 1D, 13 species EAST problem: pressure evolution during full shock tube length calculation on two grids with $\Delta x = 10^{-3}$ m and 5×10^{-4} m. Zoom of snapshots for $t = 1 \times 10^{-4}$ s and 2.5×10^{-4} s (top row), 5×10^{-4} s and 7×10^{-4} s (bottom row).

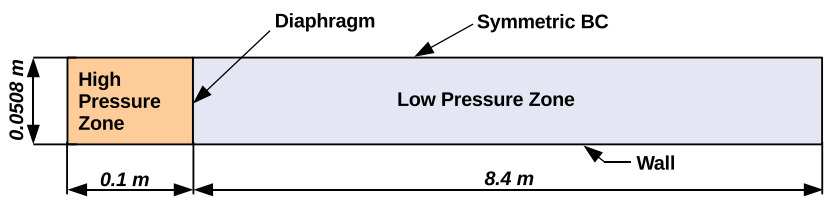

Fig. 12. Computational domain for the 2D EAST problem.

is negligible. However, there is some difference in the vicinity of the contact (e.g. compare the plots near $x = 2$ m on the second subfigure). During the flow evolution the rarefaction wave reflects from the left boundary and hits the shock at approximately $t = 7 \times 10^{-4}$ s; see the last subfigure.

Note that the high order nonlinear filter schemes using the Roe flux (except ACMTVD) are not stable for the EAST simulations. The high order subcell resolution method is not applicable for this multi-reaction and multi-species problem.

4.4. 2D EAST simulation

For the 2D case the computational domain in y is half of the 2D shock tube height. It has total length 8.5 m and height 0.0508 m (see Fig. 12). Other parameters and initial conditions of the high and low pressure regions are the same as for the 1D case. The bottom boundary is treated as an isothermal wall with the constant temperature $T_{wall} = 300$ K. The top boundary is treated as a symmetrical boundary condition.

In the x-direction both uniform and non-uniform grids are used for these simulations. For uniform grids the same strategy is applied in the x-direction as for the 1D case. For non-uniform grids the shock and shear locations are computed for each time step, and the grid points are clustered in the x-direction between the shear and shock locations with some tolerance to avoid interpolation errors during the re-grid process. This clustered portion of the grid moves as time advances.

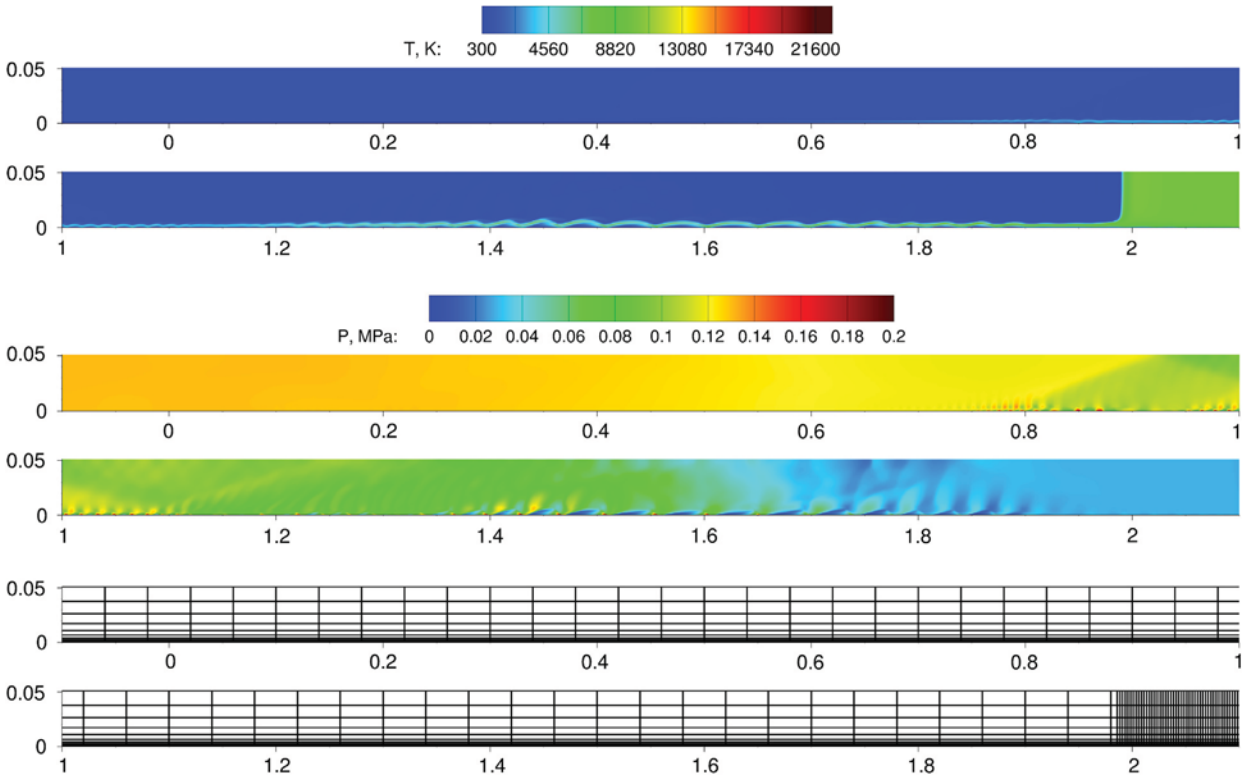

Fig. 13. 2D, 13 species EAST simulation using TVD for $CFL = 0.7$ on a grid with clustering between shear and shock for $t_{end} = 2.125 \times 10^{-4}$ s. From top to bottom: temperature contours, pressure contours and grid (shown each 50th line in X and each 10th line in Y). The shock location is $x_s = 2.1$ m.

A grid stretching is also applied to smooth the transition from the coarse to the fine grid zone. At each time step the shock and shear locations are analyzed. If the shock/shear positions change by a prescribed distance, a re-grid is invoked and the data is interpolated onto the new grid. Note that in our case the interpolation is needed only in the vicinity of the transition between coarse and fine grid zones. The shock and shear locations are computed far away from the boundary layer. However, as the boundary layer develops, the shear layer becomes more curved so that the tolerance for the shear side of the grid-clustering zone is increased. In the y-direction all grids use the same stretching algorithm so that the grid points are clustered in the vicinity of the boundary layer.

The temperature and pressure contours computed for the time $t_{end} = 2.125 \times 10^{-4}$ s together with the computational grid are shown in Fig. 13. The total computation up to given t_{end} took approximately 7 days on a maximum of 2048 CPUs (less number of CPUs is required for the early stages of the computation when the grid size is small). The solution is obtained on the grid with clustering between the shear ($x = 1.98$ m) and the shock ($x = 2.1$ m). For the grid in Fig. 13 only every 50th line in X and every 10th line in Y are shown. The grid spacing parameters are $\Delta x_{min} = 5 \times 10^{-5}$ m, $\Delta x_{max} = 8 \times 10^{-4}$ m, and $\Delta y_{min} = 10^{-5}$ m. At the given t_{end} the grid size is 5106×121. The flow behind the shock has a complex structure which includes Tollmien–Schlichting waves which noticeably develop at approximately $t = 3 \times 10^{-5}$ s. Some details of the flow structure development are shown in Figs. 14 and 15. Fig. 14 shows the pressure contours for the time $t_{end} = 1.512 \times 10^{-4}$ s between $x = 0.7$ m and $x = 1.3$ m. Fig. 15 shows the pressure and temperature contours for the time $t_{end} = 2.125 \times 10^{-4}$ s between $x = 1.4$ m and $x = 1.6$ m. The complexity of the flow structure shown on these figures implies a high demand on the accuracy of the numerical computation. For the chosen grid the simulation has already revealed a Tollmien–Schlichting-like instability complex pattern near the wall.

For this 2D test case it is not practical to obtain a very accurate reference solution due to the CPU-intensive nature of the problem. Here, three levels of refinement are conducted. Fig. 16 shows the computed temperature contour results at time $t_{end} = 10^{-5}$ s using $CFL = 0.7$ with TVD for three levels of x- and y-direction grid refinement. The top row shows three x-direction grid refinements of 601×121, 1201×121, and grid clustering between shear and shock in the x-direction of 691×121. The minimum grid step in the x-direction for the grid clustering is $\Delta x_{min} = 5 \times 10^{-5}$ m. All y grids use boundary grid stretching with a minimum of $\Delta y = 10^{-5}$ m. The bottom row shows the same two x-direction grid refinements 1201×121 and grid clustering between shear and shock in the x-direction of 691×121 (fine block). All y grids use boundary grid stretching with a minimum of $\Delta y = 5 \times 10^{-6}$ m. Comparing the two rows of the grid refinement study indicates that refining the x-direction grid while keeping the y-direction the same has a big effect on the locations of the shear and shock. This is due to the fact that aside from inside the boundary layer, the shear and shock are nearly one dimensional. However,

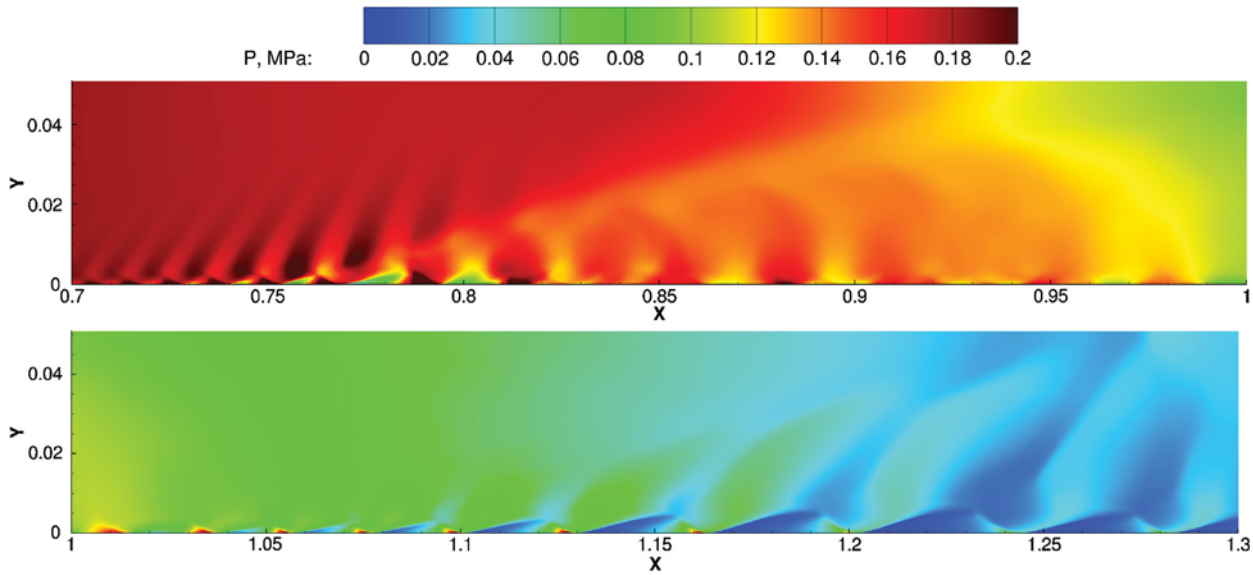

Fig. 14. 2D, 13 species EAST simulation using TVD for $CFL = 0.7$ on a grid with clustering between shear and shock. Pressure contours for $t_{end} = 1.512 \times 10^{-4}$ s.

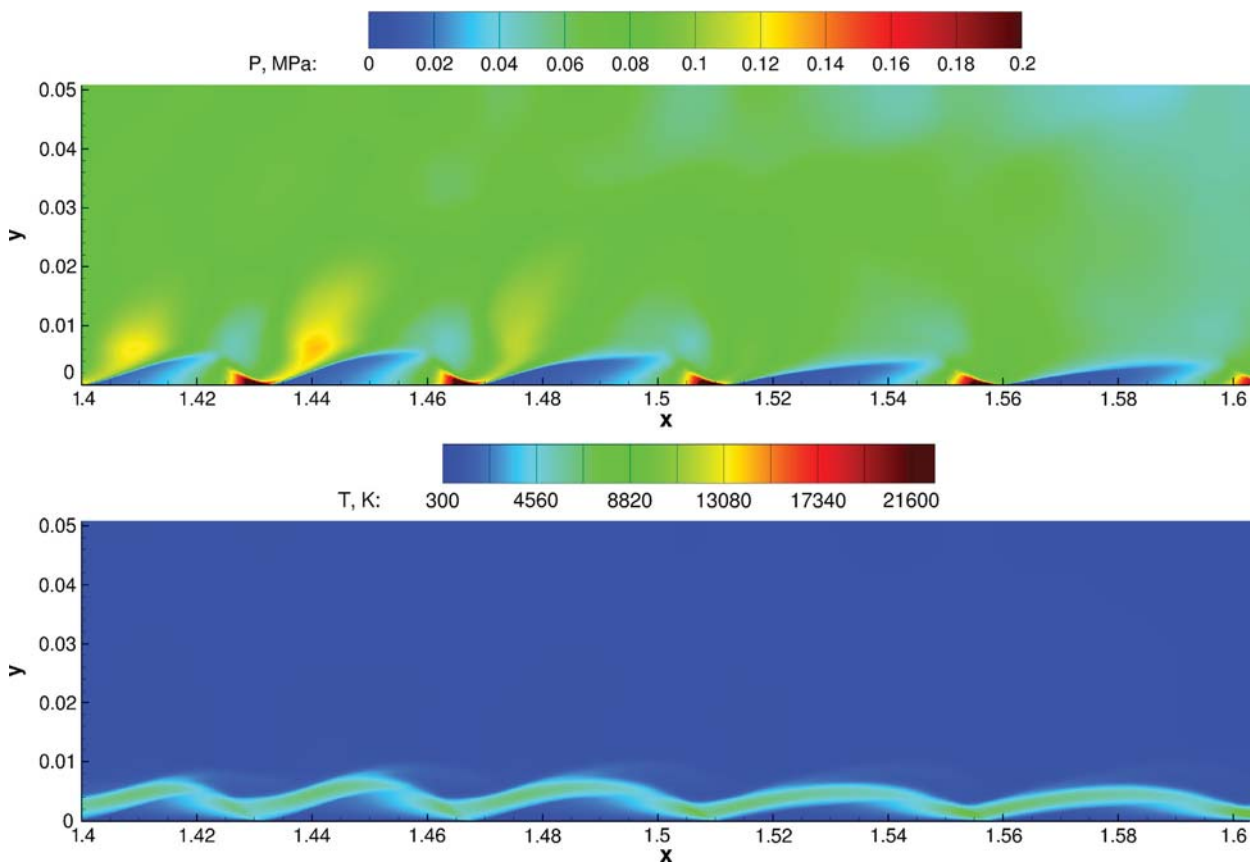

Fig. 15. 2D, 13 species EAST simulation using TVD for $CFL = 0.7$ on a grid with clustering between shear and shock. Pressure (top) and temperature (bottom) contours for $t_{end} = 2.125 \times 10^{-4}$ s.

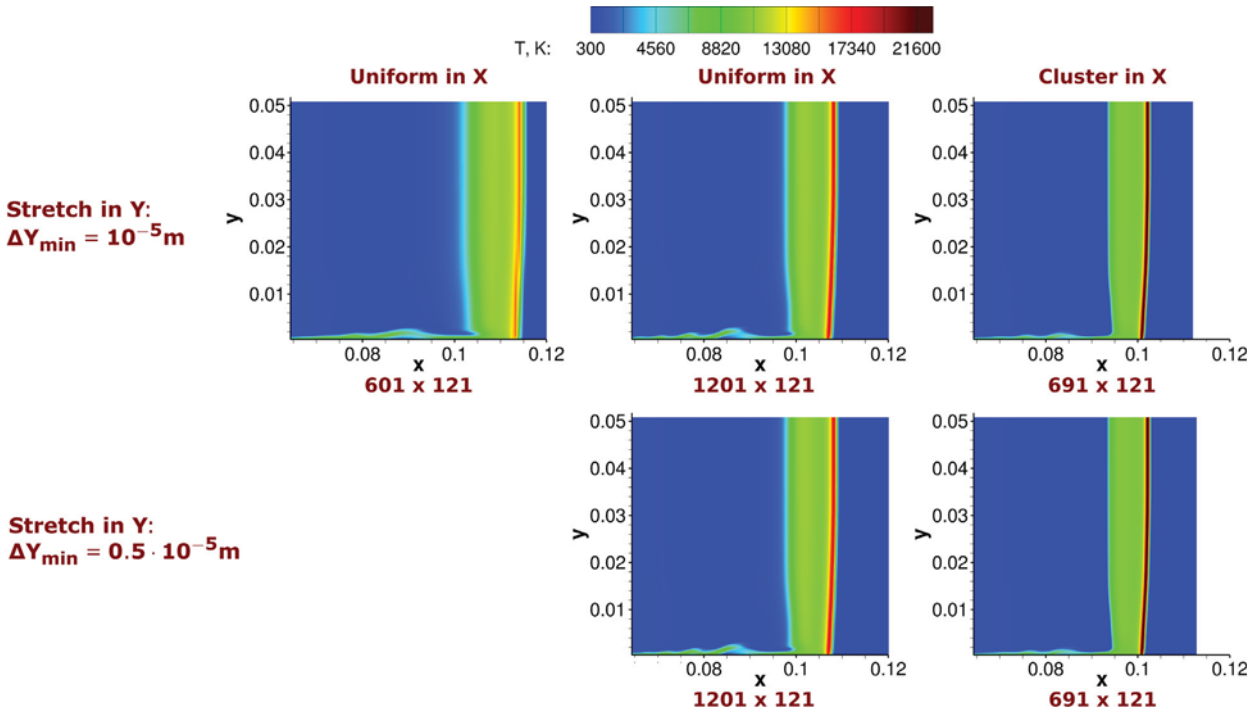

Fig. 16. 2D, 13 species EAST simulation using TVD for $CFL = 0.7$ and $t_{end} = 10^{-5}$ s: Top row: Three x-direction grid refinements: 601×121, 1201×121 and grid clustering between shear and shock in the x-direction (691×121 total). All y-grids use boundary grid stretching with a minimum of $\Delta y = 10^{-5}$ m. Bottom row: Two x-direction grid refinements: 1201×121 and grid clustering between shear and shock in the x-direction (691×121 total). All y-grids use boundary grid stretching with a minimum of $\Delta y = 5 \times 10^{-6}$ m.

Table 3
Shock and Shear maximum temperature grid dependence at time $t_{end} = 10^{-5}$ s. N_x indicates the grid spacing in the x-direction. The last two columns are grid clustering results for two different minimum y-grid stretching.

Grid N_x	601	1201	1201	691	691
Cluster in x	no	no	no	yes	yes
Min $\Delta y, m$	10^{-5}	10^{-5}	5×10^{-6}	10^{-5}	5×10^{-6}
Shock T_{max}, K	15,846	18,851	18,848	25,098	25,015
Shear T_{max}, K	11,301	11,203	11,203	10,598	10,598

comparing the last two columns of the grid refinement study indicates that refining the y-direction grid while keeping the x-direction the same has no effect on the locations of the shear/shock, but improves the boundary layer prediction.

As in the 1D EAST simulation, the discontinuity locations shift as the x-direction grid is refined, and the distance between the shear and the shock shrinks as the grid is refined. The shear and shock strengths are also different. Table 3 indicates the maximum shear and contact temperature for each set of grids. For the minimum grid stretching of $\Delta y = 10^{-5}$ m, the maximum shear temperature is 11,300 K, and the maximum shock temperature is 15,846 K for the 601×121 grid. However, the shear and shock strengths have a maximum shear temperature of 11,200 K and a maximum shock temperature of 18,851 K for the 1201×121 grid. For the stretched grid the shear and shock strengths have a maximum shear temperature of 10,600 K and maximum shock temperature of 25,098 K. As we decrease the minimum grid stretching to $\Delta y = 5 \times 10^{-6}$ m, the shear and shock strengths have a maximum shear temperature of 11,200 K and a maximum shock temperature of 18,848 K for the 1201×121 grid. For the stretched grid the shear and shock strengths have a maximum shear temperature of 10,600 K and a maximum shock temperature of 25,015 K. Aside from the different shock/shear locations, the results in the last column show that the maximum temperature at the shock location is higher than the result indicated in the middle and the first columns.

To ensure that grid clustering with $\Delta x_{min} = 5 \times 10^{-5}$ m is enough in terms of shock location error, we performed a computation on a grid twice-refined in the x-direction. The comparison of these results and a similar computation for the 1D problem are shown in Fig. 17. The 2D result profiles are taken on the upper boundary of the computational domain, where they have the best correspondence with the 1D case. The 2D results with the same Δx but different values of Δy almost coincide. The difference in the shock location for all five profiles does not exceed 1%. Note that these 2D computations are expected to have a slightly smaller shock speed than in the 1D case with the same grid resolution because of the shock-boundary layer interaction. This is confirmed by Fig. 17.

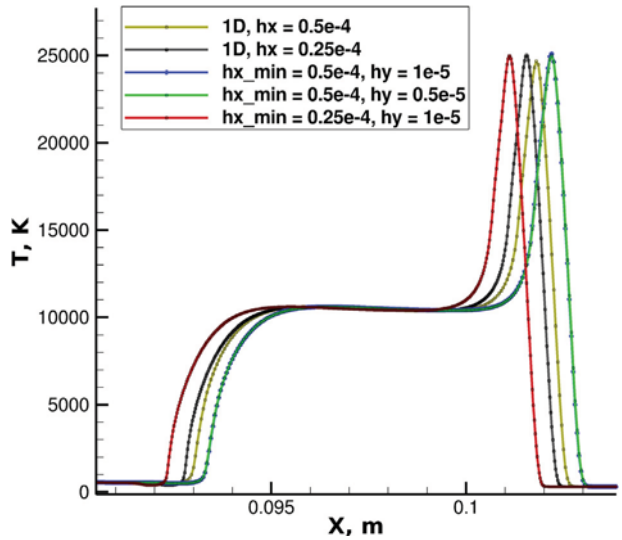

Fig. 17. 1D and 2D, 13 species EAST simulations using TVD for $t_{end} = 3.25 \times 10^{-5}$ s: 1D, $\Delta x = 5 \times 10^{-5}$ m, 1D, $\Delta x = 2.5 \times 10^{-5}$ m, 2D, $\Delta x_{min} = 5 \times 10^{-5}$ m, $\Delta y_{min} = 10^{-5}$ m, 2D, $\Delta x_{min} = 5 \times 10^{-5}$ m, $\Delta y_{min} = 5 \times 10^{-6}$ m, 2D, $\Delta x_{min} = 2.5 \times 10^{-5}$ m, $\Delta y_{min} = 10^{-5}$ m. All 1D simulations are on a uniform grid and all 2D simulations are on grids with clustering between shear and shock.

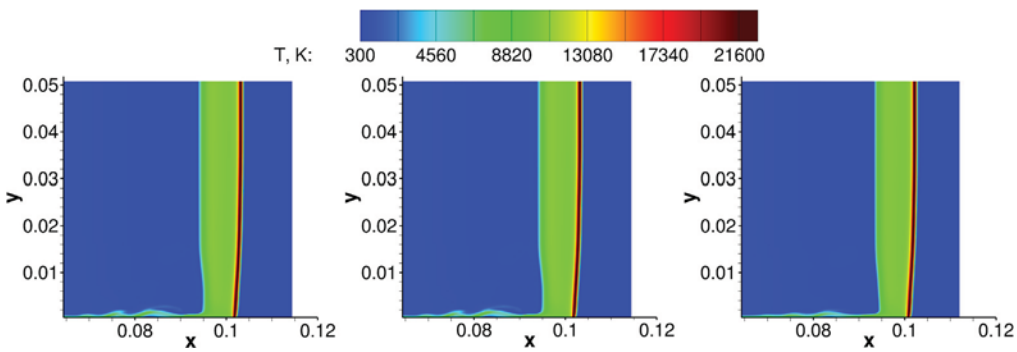

Fig. 18. 2D, 13 species EAST simulation for $t_{end} = 10^{-5}$ s on the same grid with refinement between the shear and the shock: WENO5-llf for $CFL = 0.2$ (left), WENO5P-llf for $CFL = 0.4$ (center) and TVD $CFL = 0.7$ (right).

The comparison among three numerical schemes is shown in Fig. 18. The three methods are regular TVD for $CFL = 0.7$, regular WENO5 with Lax–Friedrichs flux (WENO5-llf) for $CFL = 0.2$ and a positivity preserving version of WENO5-llf [42], designated as WENO5P-llf, for $CFL = 0.4$. It is well known that WENO-llf is very diffusive. This results in larger errors in the shock location in comparison with TVD, as can be observed in Fig. 18. WENO5P-llf obtains results similar to regular WENO5-llf, but it appears to be stable even for higher CFL numbers for which regular WENO5-llf obtains an oscillatory solution.

5. Conclusions

Studies indicate that using the same temporal discretization, solving the fully coupled reacting flow equations with stiff source terms and discontinuities for the EAST related flow model is not stable even using a very small CFL. Employing the fractional step approach by the Strang splitting in solving the reacting flow equations is more stable and allows a computational feasible CFL number for this viscous flow. Based on the knowledge gained from Yee et al. (2013) as a guide, the authors were able to reveal new results on some physical understanding, computational accuracy, instability and spurious numerics of this type of hypersonic nonequilibrium flow.

For the first time, we have presented a realistic hypersonic nonequilibrium flow that mimics the spurious behavior of more simple model problems that allow systematic nonlinear analysis. The 2D unsteady computation has been conducted for a long time evolution (physical time up to 2.125E-4 s) which corresponds to more than 2 meters of the shock tube length; see Figs. 13–15. Previous studies by other investigators encountered instability at a very early stage of time evolution (private communication with the NASA EAST experimental/computational group, 2013). For the first time, our computations reveal the Tollmien–Schlichting-like instability complex flow patterns at the boundary layer by the 2D viscous, 13 species model.

The present study demonstrates some important numerical challenges affecting the accuracy of 1D and 2D numerical solutions in simulations of NASA EAST experiments. In the early stages of the time evolution at around $t = 10^{-5}$ s the importance of obtaining very high accuracy of the discontinuities, in order to avoid an overestimation of the shock velocity, has been shown. For the 2D case, to obtain high resolution results, a moving grid with grid clustering only in key regions of the computational domain is needed in order to avoid the use of the full computational domain and unnecessary grid clustering for the entire time evolution. The precise cause of the observed grid-dependence on discontinuity locations of the computed solution is not fully understood and requires further investigation. One conjecture for the spurious behavior might be the stiff source terms, or, at least, the grid dependence may be amplified when the stiffness of the considered Ω_s is high enough. As discussed in Refs. [4,8] the level of grid- and scheme-dependence for obtaining the correct locations of discontinuities is normally dictated by the degree of stiffness of the source terms and the accuracy and amount of numerical dissipation contained in the scheme.

The present study also indicates the danger in practical numerical simulations for problems containing stiff source terms where there is no reliable means of assessing the accuracy of the computed result other than by extreme grid refinement, which may be beyond the capability of current supercomputers. Another alternative would be to develop methods that obtain the correct speed of discontinuities on coarse grids, e.g. using ideas similar to one proposed by Wang et al. [4] with further development for multi-species and multi-reaction systems. This approach might be very useful when there is a need to perform 3D computations for such experimental facilities as EAST. Knowledge gained will provide guidance for future 3D CFD simulations. Although simplified viscous 1D and 2D EAST simulations show a trend similar to our previous inviscid studies, more advanced simulations of EAST may require further systematic analysis. Future investigation including the comparison with the experimental data is planned.

Acknowledgements

The support of the DOE/SciDAC SAP grant DE-AI02-06ER25796 is acknowledged. The work was performed by the first author as a postdoctoral fellow at the Center for Turbulence Research, Stanford University. Financial support from the NASA Fundamental Aeronautics (Hypersonics) program for the second, third, fourth and fifth authors is gratefully acknowledged.

References

[1] B. Cruden, R. Martinez, J. Grinstead, J. Olejniczak, Simultaneous vacuum-ultraviolet through near-IR absolute radiation measurement with spatiotemporal resolution in an electric arc shock tube, in: 41st AIAA Thermophysics Conference, San Antonio, TX, June 2009, 2009, AIAA-2009-4240.
[2] M. Panesi, Y. Babou, O. Chazot, Predictions of nonequilibrium radiation: analysis and comparison with EAST experiments, in: 40th Thermophysics Conference, Seattle, Washington, 23–26 June 2008, 2008, AIAA-2008-3812.
[3] R. LeVeque, H.C. Yee, A study of numerical methods for hyperbolic conservation laws with stiff source terms, J. Comput. Phys. 86 (1990) 187–210.
[4] W. Wang, C.-W. Shu, H.C. Yee, B. Sjögreen, High order finite difference methods with subcell resolution for advection equations with stiff source terms, J. Comput. Phys. 231 (2012) 190–214.
[5] D. Griffiths, A. Stuart, H.C. Yee, Numerical wave propagation in hyperbolic problems with nonlinear source terms, SIAM J. Numer. Anal. 29 (1992) 1244–1260.
[6] A. Lafon, H.C. Yee, Dynamical approach study of spurious steady-state numerical solutions for nonlinear differential equations, Part III: The effects of nonlinear source terms in reaction-convection equations, Comput. Fluid Dyn. 6 (1996) 1–36.
[7] H.C. Yee, B. Sjögreen, C.-W. Shu, W. Wang, T. Magin, A. Hadjadj, On numerical methods for hypersonic turbulent flows, in: Proc. of ESA 7th Aerothermodynamics Symposium, Site Oud Sint-Jan, Brugge, Belgium, 9–12 May 2011, 2011.
[8] H.C. Yee, D.V. Kotov, W. Wang, C.-W. Shu, Spurious behavior of shock-capturing methods: problems containing stiff source terms and discontinuities, in: Proceedings of the ICCFD7, The Big Island, Hawaii, 9–13 July 2012, 2012.
[9] H.C. Yee, D.V. Kotov, W. Wang, C.-W. Shu, Spurious behavior of shock-capturing methods by the fractional step approach: problems containing stiff source terms and discontinuities, J. Comput. Phys. 241 (2013) 266–291.
[10] E. McCorkle, H. Hassan, Study of radiation in electric arc shock tubes, in: 10th AIAA/ASME Joint Thermophysics and Heat Transfer Conference, Chicago, Illinois, 28 June–1 July 2010, 2010.
[11] H.C. Yee, B. Sjögreen, High order filter methods for wide range of compressible flow speeds, in: Proc. of ICOSAHOM 09 (International Conference on Spectral and High Order Methods), Trondheim, Norway, 22–26 June 2009, 2009.
[12] B. Sjögreen, H.C. Yee, Multiresolution wavelet based adaptive numerical dissipation control for shock-turbulence computation, J. Sci. Comput. 20 (2004) 211–255.
[13] H.C. Yee, B. Sjögreen, A. Hadjadj, Comparative study of high order schemes for LES of temporal-evolving mixing layers, in: Proc. of ASTRONUM-2010, San Diego, Calif., 13–18 June 2010, 2010.
[14] W. Wang, H.C. Yee, B. Sjögreen, T. Magin, C.-W. Shu, Construction of low dissipative high-order well-balanced filter schemes for nonequilibrium flows, J. Comput. Phys. 230 (2011) 4316–4335.
[15] H.C. Yee, A Class of High-Resolution Explicit and Implicit Shock-Capturing Methods, VKI Lecture Series 1989-04, 1989.
[16] H.C. Yee, G.H. Klopfer, J.-L. Montagne, High-resolution shock-capturing schemes for inviscid and viscous hypersonic flows, J. Comput. Phys. 88 (1990) 31–61.
[17] G.-S. Jiang, C.-W. Shu, Efficient implementation of weighted ENO schemes, J. Comput. Phys. 126 (1996) 202–228.
[18] F. Ducros, F. Laporte, T. Soulères, V. Guinot, P. Moinat, B. Caruelle, High-order fluxes for conservative skew-symmetric-like schemes in structured meshes: application to compressible flows, J. Comput. Phys. 161 (2000) 114–139.
[19] H.C. Yee, B. Sjögreen, Development of low dissipative high order filter schemes for multiscale Navier–Stokes/MHD systems, J. Comput. Phys. 225 (2007) 910–934.
[20] G. Strang, On the construction and comparison of difference schemes, SIAM J. Numer. Anal. 5 (1968) 506–517.
[21] A. Harten, ENO schemes with subcell resolution, J. Comput. Phys. 83 (1989) 148–184.
[22] P. Olsson, J. Oliger, Energy and maximum norm estimates for nonlinear conservation laws, Tech. Rep. 94.01, RIACS, 1994.
[23] H.C. Yee, M. Vinokur, M. Djomehri, Entropy splitting and numerical dissipation, J. Comput. Phys. 162 (2000) 33–81.

[24] H.C. Yee, B. Sjögreen, Designing adaptive low dissipative high order schemes for long-time integrations, in: D.D.B. Geurts (Ed.), Turbulent Flow Computation, Kluwer Academic, 2002.
[25] B. Sjögreen, H.C. Yee, On skew-symmetric splitting and entropy conservation schemes for the Euler equations, in: Proc. of the 8th Euro. Conf. on Numerical Mathematics & Advanced Applications (ENUMATH), Uppsala University, Uppsala, Sweden, June 29–July 2 2009, 2009.
[26] A. Honein, Numerical aspects of compressible turbulence simulations, Ph.D. thesis, Stanford University, 2004.
[27] P. Olsson, Summation by parts, projections, and stability. I, Math. Comput. 64 (1995) 1035–1065.
[28] B. Sjögreen, H.C. Yee, On tenth-order central spatial schemes, in: Proceedings of the Turbulence and Shear Flow Phenomena 5 (TSFP-5), Munich, Germany, 27–29 August 2007, 2007.
[29] M. Vinokur, H.C. Yee, Extension of efficient low dissipative high-order schemes for 3D curvilinear moving grids, in: Frontiers of Computational Fluid Dynamics, World Scientific, 2002, pp. 129–164.
[30] H.C. Yee, N. Sandham, M. Djomehri, Low dissipative high order shock-capturing methods using characteristic-based filters, J. Comput. Phys. 150 (1999) 199–238.
[31] H.C. Yee, B. Sjögreen, Adaptive filtering and limiting in compact high order methods for multiscale gas dynamics and MHD systems, Comput. Fluids 37 (2008) 593–619.
[32] D.V. Kotov, H.C. Yee, W. Wang, C.-W. Shu, On spurious numerics in solving reactive equations, in: Proceedings of the ASTRONUM-2012, The Big Island, Hawaii, 24–28 June 2012, 2012.
[33] C. Helzel, R. LeVeque, G. Warneke, A modified fractional step method for the accurate approximation of detonation waves, SIAM J. Sci. Stat. Comput. 22 (1999) 1489–1510.
[34] L. Tosatto, L. Vigevano, Numerical solution of under-resolved detonations, J. Comput. Phys. 227 (2008) 2317–2343.
[35] H.C. Yee, D.V. Kotov, B. Sjogreen, Numerical dissipation and wrong propagation speed of discontinuities for stiff source terms, in: Proceedings of the ASTRONUM-2011, Valencia, Spain, 13–17 June 2011, 2011.
[36] D.V. Kotov, H.C. Yee, B. Sjögreen, Comparative study of high-order positivity-preserving WENO schemes, Tech. rep., Center for Turbulence Research, Stanford, California, 2012.
[37] A. Lani, B. Sjögreen, H.C. Yee, W. Henshaw, Variable high-order multiblock overlapping grid methods for mixed steady and unsteady multiscale viscous flows, Part II: Hypersonic nonequilibrium flows, Commun. Comput. Phys. 13 (2013) 583–602.
[38] B. Sjögreen, H.C. Yee, Variable high order multiblock overlapping grid methods for mixed steady and unsteady multiscale viscous flows, Commun. Comput. Phys. 5 (2009) 730–744.
[39] M. Panesi, T. Magin, A. Bourdon, A. Bultel, O. Chazot, Analysis of the Fire II flight experiment by means of a collisional radiative model, J. Thermophys. Heat Transf. 23 (2) (April–June 2009) 236–248.
[40] M. Panesi, T. Magin, A. Bourdon, A. Bultel, O. Chazot, Study of electronically excited state populations of atoms and molecules predicted by means of a collisional-radiative model for the Fire II flight experiment, J. Thermophys. Heat Transf. 25 (25) (2011) 361–374.
[41] A.C. Hindmarsh, ODEPACK, a systematized collection of ODE solvers, in: R.S. Stepleman, et al. (Eds.), Scientific Computing, North-Holland, Amsterdam, 1983, pp. 55–64.
[42] X. Zhang, C.-W. Shu, Positivity-preserving high order finite difference WENO schemes for compressible Euler equations, J. Comput. Phys. 231 (2012) 2245–2258.
[43] X. Hu, N. Adams, C.-W. Shu, Positivity-preserving flux limiters for high-order conservation schemes, J. Comput. Phys. 242 (2013) 169–180.
[44] P.A. Jacobs, Numerical simulation of transient hypervelocity flow in an expansion tube, Comput. Fluids 23 (1994) 77–101.
[45] P. Petrie-Repar, Numerical simulation of diaphragm rupture, Ph.D. thesis, University of Queensland, 1997.